doi: 10.82124/CEAS-GNC-2026-023 CEAS-GNC-2026-023

Analytical Algorithms for GNSS-Independent Position and Heading Determination Using Stellar Sensors

Guillermo Pacheco-Ramos *Assistant Professor, Universidad de Sevilla, Escuela Técnica Superior de Ingeniería, Seville, Spain. gpacheco@us.es*

Francisco Gavilan *Associate Professor, Universidad de Sevilla, Escuela Técnica Superior de Ingeniería, Seville, Spain. fgavilan@us.es*

Rafael Vazquez *Professor, Universidad de Sevilla, Escuela Técnica Superior de Ingeniería, Seville, Spain. rvazquez1@us.es*

Diego Zarco Vaz *GNC Engineer, SOLAR MEMS Technologies, La Rinconada, Spain. diego.zarco@solar-mems.com*

Manuel Rodríguez Halcón *Chief Technical Officer, SOLAR MEMS Technologies, La Rinconada, Spain. manuel.rodriguez@solar-mems.com*

ABSTRACT

The increasing reliance on Global Navigation Satellite Systems (GNSS) has highlighted critical vulnerabilities to jamming and spoofing, driving demand for assured Position, Navigation and Timing (A-PNT) capabilities in GNSS-denied environments. This paper presents analytical algorithms for autonomous navigation using stellar sensors to provide GNSS-independent positioning and heading determination.

Two complementary approaches are developed: sun sensor-based position determination through analytical solution of geometric equations relating measured solar vectors to ephemeris data, and star tracker-based simultaneous position and heading estimation exploiting quaternion attitude measurements. For the latter, a novel reference frame modification incorporating yaw into the Earth-to-navigation transformation enables direct extraction of latitude, longitude, and heading from quaternion data through Euler angle decomposition.

Error propagation analysis via Jacobian linearization quantifies the influence of sensor noise, attitude errors, and geophysical effects. Monte Carlo simulations with realistic sensor characteristics validate the analytical error models. Results demonstrate positioning accuracies of several kilometers for sun sensors and sub-kilometer for star trackers, with the latter achieving arcsecond-level heading precision. Latitude-dependent performance characteristics and geometric sensitivity factors are analyzed, providing design guidelines for GNSS-independent navigation systems.

Keywords: stellar navigation, celestial navigation, GNSS-denied navigation, assured PNT, inertial navigation

1 Introduction

The widespread adoption of Global Navigation Satellite Systems has created critical dependencies in both civilian and military applications. Recent developments in electronic warfare capabilities and demonstrated vulnerability of GNSS signals to jamming and spoofing have renewed interest in alternative

navigation technologies [1, 2]. Stellar navigation, historically employed in aerospace applications, offers a passive and unjammable alternative for assured positioning services.

The strategic importance of GNSS-independent navigation was demonstrated during the Cold War era, when advanced aircraft like the SR-71 Blackbird employed the Nortronics NAS-14V2 astroinertial navigation system to maintain course accuracy within 90 meters over multi-hour missions [3]. Similarly, strategic bombers including the B-52 and B-2 incorporated stellar navigation systems for precision guidance in contested environments [4]. Maritime applications have long relied on celestial navigation, with modern submarines continuing to use stellar updates for inertial navigation system corrections during surfaced operations [5].

Contemporary research has explored stellar navigation applications for unmanned aerial vehicles operating in GNSS-denied environments [6], terrestrial platforms requiring assured navigation [7], and integration with modern inertial measurement units for enhanced positioning accuracy [8]. The resurgence of interest in stellar navigation reflects growing concerns about GNSS vulnerabilities in both military and critical civilian infrastructure applications.

This paper develops analytical algorithms for two primary stellar sensor configurations: sun sensors for position determination and star trackers for simultaneous position and heading estimation. The analytical approach provides computational efficiency suitable for real-time applications while enabling closed-form error analysis for performance prediction. The main contribution lies in the development of a quaternion-based algorithm for star trackers that directly extracts geodetic coordinates and heading through a modified reference frame hierarchy, avoiding iterative optimization procedures.

Section 2 establishes the mathematical foundations including reference frames and attitude representations. Section 3 presents the sun sensor algorithm and error analysis. Section 4 details the star tracker methodology with emphasis on the quaternion-based approach. Section 5 provides Monte Carlo validation results demonstrating positioning accuracies and performance characteristics. Section 6 summarizes key findings and discusses operational implications.

2 Preliminary Concepts

This section establishes the mathematical framework required for the subsequent algorithmic development, including reference frame definitions, coordinate transformations, and attitude representations. All rotations are defined as passive transformations between reference frames, and quaternion operations follow the corresponding convention and multiplication order consistent with this definition.

2.1 Reference Frames and Transformations

The stellar navigation algorithms require coordinate transformations through a hierarchy of reference frames. The primary frames employed are:

- **Earth-Centered Inertial (ECI):** Geocentric frame with origin at Earth's center, z-axis aligned with Earth's rotation axis, and x-axis pointing toward the vernal equinox. The International Celestial Reference Frame (ICRF) provides the practical realization through precise extragalactic radio source positions.
- **Earth-Centered Earth-Fixed (ECEF):** Geocentric frame rotating with Earth. The z-axis coincides with the ECI z-axis, while the x-axis intersects the Greenwich meridian. The International Terrestrial Reference Frame (ITRF) realizes this system with millimeter-level accuracy. The transformation from ECI to ECEF accounts for Earth rotation through Greenwich Sidereal Time (GST).
- **Local Navigation Frame (NED):** North-East-Down frame tangent to the reference ellipsoid at the observer's location, defined by geodetic latitude ϕ and longitude λ.

- **Body-Fixed Frame (BFS):** Frame attached to the vehicle with axes aligned according to aerospace conventions (typically x-forward, y-right, z-down). Vehicle attitude relative to NED is parameterized by Euler angles: yaw ψ, pitch θ, and roll φ.
- **Sensor Frame (SF):** Frame fixed to the stellar sensor with known transformation relative to BFS, characterized by mounting alignment matrix $\mathbf{C}_b^s$.

The complete transformation chain from inertial to sensor frame is expressed as:

$$\mathbf{v}^s = \mathbf{C}_b^s \mathbf{C}_g^b \mathbf{C}_e^g \mathbf{C}_i^e \mathbf{v}^i \tag{1}$$

where $\mathbf{C}_A^B$ denotes the direction cosine matrix (DCM) transforming vectors from frame A to frame B. The ECEF-to-NED transformation $\mathbf{C}_e^g(\phi, \lambda)$ contains the unknown observer position, while $\mathbf{C}_g^b(\psi, \theta, \varphi)$ encodes the vehicle attitude.

2.2 Attitude Representations

Three attitude representations are employed: direction cosine matrices, Euler angles, and quaternions. Each offers distinct computational advantages for specific algorithmic stages.

Direction Cosine Matrices: Orthogonal 3×3 matrices representing rotations. For a Z-Y-X Euler sequence (yaw-pitch-roll), the DCM defining the orientation of the body frame respect to the navigation frame can be written as:

$$\mathbf{C}_g^b(\psi, \theta, \varphi) = \mathbf{C}_x(\varphi)\mathbf{C}_y(\theta)\mathbf{C}_z(\psi) \tag{2}$$

where $\mathbf{C}_i(\alpha)$ denotes elementary rotation about axis i.

Quaternions: Unit quaternions $\mathbf{q} = [q_0, q_1, q_2, q_3]^T$ with $|\mathbf{q}| = 1$ provide singularity-free attitude representation. The quaternion product $\mathbf{q}_C = \mathbf{q}_A \star \mathbf{q}_B$ composes rotations, where $\mathbf{q}_A$ transforms from frame A to B and $\mathbf{q}_B$ from B to C. Conversion between DCM and quaternion representations employs the Euler-Rodriguez formula:

$$\mathbf{C}(\mathbf{q}) = (q_0^2 - \mathbf{q}_v^T\mathbf{q}_v)\mathbf{I} + 2\mathbf{q}_v\mathbf{q}_v^T - 2q_0[\mathbf{q}_v]_\times \tag{3}$$

where $\mathbf{q}_v = [q_1, q_2, q_3]^T$ is the vector part and $[\cdot]_\times$ denotes the skew-symmetric matrix operator.

Euler Angles: Minimal three-parameter representation subject to singularities at specific orientations (gimbal lock). Extraction from DCM for the Z-Y-X sequence:

$$\theta = -\arcsin(C_{13}), \quad \theta \in [-90°, 90°] \tag{4}$$

$$\psi = \text{atan2}(C_{12}, C_{11}) \tag{5}$$

$$\varphi = \text{atan2}(C_{23}, C_{33}) \tag{6}$$

where C_{ij} denotes the (i, j) element of the DCM defining the vehicle attitude C_g^b.

2.3 Celestial Ephemerides

Precise celestial body positions are obtained from the SPICE (Spacecraft, Planet, Instrument, C-matrix, Events) system developed by NASA's Navigation and Ancillary Information Facility [11]. The system provides high-fidelity ephemerides accounting for relativistic effects, light-time corrections, and stellar aberration. For the sun, ephemeris accuracy is sub-kilometer at Earth distances. Star positions are referenced to the ICRF with milliarcsecond precision.

2.4 Error Modeling

Measurement errors are modeled as zero-mean Gaussian random variables. For attitude errors, small-angle approximations enable linearization:

$$\mathbf{C}_{\hat{b}}^{b} \approx \mathbf{I} - [\delta\boldsymbol{\alpha}]_{\times} \tag{7}$$

where $\delta\boldsymbol{\alpha}$ is the small rotation error vector. Error propagation through the transformation chain is analyzed via Jacobian matrices, yielding covariance expressions for position and heading estimates as functions of sensor error statistics.

3 Sun Sensor Position Determination

This section presents an analytical algorithm for determining observer geodetic coordinates using sun sensor measurements. The approach solves a system of geometric equations relating measured solar direction vectors to theoretical ephemeris predictions.

3.1 Algorithm Formulation

The sun sensor measures the solar direction in the sensor frame as a unit vector $\mathbf{v}_{\text{meas}}^{s}$ characterized by two angular measurements (α_x, α_y), defined as the complementary angles of the direction angles associated with the x- and y-components of the unit Sun vector expressed in the sensor frame:

$$\mathbf{v}_{\text{meas}}^{s} = \begin{bmatrix} \sin\alpha_x \\ \sin\alpha_y \\ \sqrt{1 - \sin^2\alpha_x - \sin^2\alpha_y} \end{bmatrix}, \tag{8}$$

assuming the Sun lies within the visible hemisphere of the sensor and Sun vector within the field of view (FOV) of the sensor.

The theoretical solar vector in ECEF frame is obtained from ephemeris data:

$$\mathbf{v}_{s}^{e}(t) = \mathbf{C}_{i}^{e}(t)\mathbf{v}_{s}^{i}(t) = \begin{bmatrix} v_x \\ v_y \\ v_z \end{bmatrix} \tag{9}$$

where $\mathbf{v}_{s}^{i}(t)$ is the sun position vector from SPICE ephemeris at time t, and $\mathbf{C}_{i}^{e}(t)$ accounts for Earth rotation through GST.

The measured vector transformed to NED frame via known attitude (ψ, θ, φ) is:

$$\mathbf{v}_{s}^{g} = (\mathbf{C}_{g}^{b})^{T}(\mathbf{C}_{b}^{s})^{T}\mathbf{v}_{\text{meas}}^{s} = \begin{bmatrix} v_N \\ v_E \\ v_D \end{bmatrix} \tag{10}$$

The fundamental geometric relationship $\mathbf{v}_s^g = \mathbf{C}_e^g(\phi, \lambda)\mathbf{v}_s^e$ yields three scalar equations. The ECEF-to-NED transformation matrix is:

$$\mathbf{C}_e^g(\phi, \lambda) = \begin{bmatrix} -\sin\phi\cos\lambda & -\sin\phi\sin\lambda & \cos\phi \\ -\sin\lambda & \cos\lambda & 0 \\ -\cos\phi\cos\lambda & -\cos\phi\sin\lambda & -\sin\phi \end{bmatrix} \tag{11}$$

Expressing this transformation as a rotation sequence

$$\text{ECEF} \xrightarrow[z_e]{\lambda} S \xrightarrow[y_S]{-\phi} S' \xrightarrow[y_{S'}]{-90^\circ} \text{NED} \tag{12}$$

and manipulating the fundamental equation yields:

$$v_N\cos\phi - v_D\sin\phi = v_z \tag{13}$$
$$-v_x\sin\lambda + v_y\cos\lambda = v_E \tag{14}$$
$$v_x\cos\lambda + v_y\sin\lambda = -v_D\cos\phi - v_N\sin\phi \tag{15}$$

Latitude Solution: Equation (13) has the form $A\cos\phi + B\sin\phi = C$ with $A = v_N$, $B = -v_D$, $C = v_z$. The general solution is:

$$\phi = \text{atan2}(-v_D, v_N) \pm \arccos\left(\frac{v_z}{\sqrt{v_N^2 + v_D^2}}\right) \tag{16}$$

being $\arccos(\cdot) \in [0^\circ, 180^\circ]$. The two solutions ϕ_1, ϕ_2, arise from the inherent trigonometric ambiguity and are resolved by enforcing the latitude range $\phi \in [-90^\circ, 90^\circ]$ and/or known approximate value of ϕ.

Longitude Solution: For each valid ϕ_j, define the auxiliary variable $C'_j = -v_D\cos\phi_j - v_N\sin\phi_j$. Equations (14)–(15) form a linear system for $\cos\lambda_j$ and $\sin\lambda_j$:

$$\begin{bmatrix} v_x & v_y \\ v_y & -v_x \end{bmatrix}\begin{bmatrix} \cos\lambda_j \\ \sin\lambda_j \end{bmatrix} = \begin{bmatrix} C'_j \\ v_E \end{bmatrix} \tag{17}$$

with solution:

$$\lambda_j = \text{atan2}\left(\frac{v_y C'_j - v_x v_E}{v_x^2 + v_y^2}, \frac{v_x C'_j + v_y v_E}{v_x^2 + v_y^2}\right) \tag{18}$$

Singular Case: A unique solution occurs when $v_z^2 = v_N^2 + v_D^2$, corresponding to solar hour angle $H_s = \pm 90^\circ$ (local apparent solar time of 06:00 or 18:00). Near these geometries, the two mathematical solutions converge, reducing numerical robustness. Practical implementations should monitor the condition number $\sqrt{v_N^2 + v_D^2}/|v_z|$ and restrict operation away from singular configurations.

3.2 Error Propagation Analysis

Position estimation errors arise from sensor measurement errors $(\delta\alpha_x, \delta\alpha_y)$, attitude determination errors $(\delta\psi, \delta\theta, \delta\varphi)$, and geophysical modeling errors (deflection of vertical, atmospheric refraction); the latter are skipped in this preliminary study. Error propagation is analyzed by linearizing the residual vector:

$$\mathbf{R}(\phi, \lambda, \psi, \theta, \varphi, \alpha_x, \alpha_y) = (\mathbf{C}_g^b)^T(\mathbf{C}_b^s)^T\mathbf{v}_{\text{meas}}^s - \mathbf{C}_e^g\mathbf{C}_i^e\mathbf{v}_s^i = \mathbf{0} \tag{19}$$

First-order Taylor expansion yields:

$$\mathbf{J}_x \delta\mathbf{x} + \mathbf{J}_p \delta\mathbf{p} = \mathbf{0} \tag{20}$$

where $\delta\mathbf{x} = [\delta\phi, \delta\lambda]^T$ are position errors, $\delta\mathbf{p} = [\delta\psi, \delta\theta, \delta\phi, \delta\alpha_x, \delta\alpha_y]^T$ are input errors, and Jacobian matrices are:

$$\mathbf{J}_x = \left[-\frac{\partial \mathbf{C}_e^g}{\partial \phi}\mathbf{v}_s^e \quad -\frac{\partial \mathbf{C}_e^g}{\partial \lambda}\mathbf{v}_s^e \right] \in \mathbb{R}^{3\times 2} \tag{21}$$

$$\mathbf{J}_p = \left[-[\mathbf{v}_{\text{meas}}^g]_\times \mathbf{T}_{\text{Euler}} \quad (\mathbf{C}_g^b)^T (\mathbf{C}_b^s)^T \frac{\partial \mathbf{v}^s}{\partial \alpha_x} \quad (\mathbf{C}_g^b)^T (\mathbf{C}_b^s)^T \frac{\partial \mathbf{v}^s}{\partial \alpha_y} \right] \in \mathbb{R}^{3\times 5} \tag{22}$$

where $\mathbf{T}_{\text{Euler}}$ transforms Euler angle errors to body-frame rotation errors.

The least-squares position error estimate is:

$$\delta\mathbf{x} = -(\mathbf{J}_x^T \mathbf{J}_x)^{-1} \mathbf{J}_x^T \mathbf{J}_p \delta\mathbf{p} \equiv \mathbf{S}\delta\mathbf{p} \tag{23}$$

The sensitivity matrix $\mathbf{S} \in \mathbb{R}^{2\times 5}$ quantifies error propagation. For Gaussian input errors with covariance $\text{Cov}(\delta\mathbf{p})$, the position error covariance is:

$$\text{Cov}(\delta\mathbf{x}) = \mathbf{S} \cdot \text{Cov}(\delta\mathbf{p}) \cdot \mathbf{S}^T \tag{24}$$

The determinant $\det(\mathbf{J}_x^T \mathbf{J}_x)$ serves as an observability metric: small values near $H_s = \pm 90°$ indicate ill-conditioning and degraded accuracy.

4 Star Tracker Position and Heading Determination

This section develops a quaternion-based analytical algorithm for simultaneous determination of observer position and vehicle heading using star tracker measurements. The key innovation is a modified reference frame hierarchy that incorporates yaw into the Earth-to-navigation transformation, enabling direct extraction of all three unknowns (ϕ, λ, ψ) through Euler angle decomposition.

4.1 Modified Reference Frame Hierarchy

Star trackers provide high-precision attitude quaternions $\mathbf{q}_{s/i}$ representing the sensor orientation relative to the inertial frame. The standard reference frame chain:

$$\mathbf{q}_{s/i} = \mathbf{q}_{e/i} \star \mathbf{q}_{g/e} \star \mathbf{q}_{b/g} \star \mathbf{q}_{s/b} \tag{25}$$

contains unknowns distributed across multiple transformations: position (ϕ, λ) in $\mathbf{q}_{g/e}$ and heading ψ (along with pitch θ and roll φ) in $\mathbf{q}_{b/g}$.

To isolate all three unknowns in a single transformation, a Front-Right-Down (FRD) navigation frame is introduced, differing from standard NED by absorbing the yaw rotation. The modified hierarchy becomes:

$$\mathbf{q}_{s/i} = \mathbf{q}_{e/i} \star \mathbf{q}_{f/e} \star \mathbf{q}_{b/f} \star \mathbf{q}_{s/b} \tag{26}$$

where the FRD frame is defined by:

$$\text{ECEF} \xrightarrow[z_e]{\lambda} S \xrightarrow[y_S]{\tilde{\phi}} S' \xrightarrow[z_{S'}]{\psi} \text{FRD} \tag{27}$$

with the modified latitude angle $\tilde{\phi} = -\phi - 90°$ ensuring $\tilde{\phi} \in [-180°, 0°]$ maps to geographic latitude $\phi \in [-90°, 90°]$. This yields a 3-2-3 Euler sequence $(\lambda, \tilde{\phi}, \psi)$ encoding position and heading.

The body-to-FRD transformation now contains only pitch and roll:

$$\mathbf{q}_{b/f} = \mathbf{q}_y(\theta) \star \mathbf{q}_x(\varphi) \tag{28}$$

where $\mathbf{q}_y(\theta)$ and $\mathbf{q}_x(\varphi)$ are elementary quaternions for rotations about y and x axes, respectively.

4.2 Analytical Solution Procedure

The algorithm proceeds in five steps:

Step 1: Inertial-to-ECEF Quaternion. Compute $\mathbf{q}_{e/i}(t)$ from the transformation matrix $\mathbf{C}_i^e(t)$ obtained via SPICE, accounting for Earth rotation at ephemeris time t.

Step 2: Body-to-FRD Quaternion. Construct $\mathbf{q}_{b/f}$ from AHRS-measured pitch and roll using Eq. (28). The AHRS provides (θ, φ) through accelerometer-based gravity sensing and gyroscope integration.

Step 3: FRD-to-ECEF Quaternion Isolation. Rearrange Eq. (26) using quaternion conjugates:

$$\mathbf{q}_{f/e} = \mathbf{q}_{e/i}^* \star \mathbf{q}_{s/i} \star \mathbf{q}_{s/b}^* \star \mathbf{q}_{b/f}^* \tag{29}$$

where $\mathbf{q}^*$ denotes quaternion conjugate. All terms on the right-hand side are known: $\mathbf{q}_{s/i}$ from star tracker, $\mathbf{q}_{s/b}$ from sensor mounting calibration, and $\mathbf{q}_{b/f}$ from Step 2.

Step 4: DCM Conversion. Convert $\mathbf{q}_{f/e}$ to direction cosine matrix $\mathbf{C}_e^f$ using the Euler-Rodriguez formula:

$$\mathbf{C}_e^f = \begin{bmatrix} c_{11} & c_{12} & c_{13} \\ c_{21} & c_{22} & c_{23} \\ c_{31} & c_{32} & c_{33} \end{bmatrix} \tag{30}$$

Step 5: Euler Angle Extraction. The 3-2-3 sequence $(\lambda, \tilde{\phi}, \psi)$ is extracted using a non-standard parameterization with middle angle restricted to $[-180°, 0°]$:

$$\tilde{\phi} = \arccos(c_{33}), \quad \tilde{\phi} \in [-180°, 0°] \tag{31}$$

$$\lambda = \text{atan2}\left(\frac{c_{32}}{\sin\tilde{\phi}}, \frac{c_{31}}{\sin\tilde{\phi}}\right) \tag{32}$$

$$\psi = -\text{atan2}\left(\frac{c_{23}}{\sin\tilde{\phi}}, \frac{c_{13}}{\sin\tilde{\phi}}\right) \tag{33}$$

Geographic latitude is recovered via $\phi = -\tilde{\phi} - 90°$. This approach provides unique solutions except at poles ($\phi = \pm 90°$), where longitude and heading become undefined—a fundamental limitation inherent to any geodetic parameterization.

4.3 Error Propagation Analysis

Position and heading errors arise from star tracker angular errors and accelerometer noise. The error propagation framework employs small-angle linearization of attitude errors.

For DCM perturbations, small body-frame rotation error $\delta\boldsymbol{\alpha}^b$ relates to matrix error via:

$$\mathbf{C}_{\hat{b}}^b \approx \mathbf{I} - [\delta\boldsymbol{\alpha}^b]_\times \tag{34}$$

Star tracker errors are modeled with anisotropic characteristics: cross-axis error σ_{xy} (typically 2 arcsec for commercial units) and about-axis error σ_z (typically 10 arcsec). The error quaternion $\mathbf{q}_{s/\hat{s}}$ is constructed from two successive small rotations.

Accelerometer errors propagate through pitch and roll determination. For noise $\delta\mathbf{f}^b$ with standard deviation σ_a, the pitch and roll error standard deviations are:

$$\sigma_\theta = \frac{\sigma_a}{g} \tag{35}$$

$$\sigma_\varphi = \frac{\sigma_a}{g\cos\theta} \tag{36}$$

showing pitch-dependent amplification of roll error.

Through the quaternion chain, the output error vector $\delta\boldsymbol{\alpha}_{\text{out}}$ (rotation error post-multiplying $\mathbf{C}_e^f$) relates to input errors via:

$$\delta\boldsymbol{\alpha}_{\text{out}} = -(\mathbf{C}_f^b)^T\delta\boldsymbol{\alpha}_{\text{att}} + (\mathbf{C}_f^b)^T(\mathbf{C}_b^s)^T\delta\boldsymbol{\alpha}_{\text{ST}} \tag{37}$$

where $\delta\boldsymbol{\alpha}_{\text{att}}$ represents AHRS attitude errors and $\delta\boldsymbol{\alpha}_{\text{ST}}$ star tracker errors.

The transformation from rotation error to Euler angle errors $[\delta\phi, \delta\lambda, \delta\psi]^T$ depends on current values of $(\hat{\phi}, \hat{\psi})$:

$$\begin{bmatrix}\delta\phi\\ \delta\lambda\\ \delta\psi\end{bmatrix} = \mathbf{A}(\hat{\phi}, \hat{\psi}) \cdot \delta\boldsymbol{\alpha}_{\text{out}} \tag{38}$$

where:

$$\mathbf{A}(\phi, \psi) = \begin{bmatrix} -\sin\psi & -\cos\psi & 0\\ \cos\psi/\cos\phi & -\sin\psi/\cos\phi & 0\\ \sin\phi\cos\psi/\cos\phi & \sin\phi\sin\psi/\cos\phi & 1\end{bmatrix} \tag{39}$$

High latitudes amplify longitude and heading errors due to the $1/\cos\phi$ factor, a geometric effect fundamental to geodetic coordinates. The covariance matrix of output errors is:

$$\text{Cov}\begin{bmatrix}\delta\phi\\ \delta\lambda\\ \delta\psi\end{bmatrix} = \mathbf{A}\cdot\mathbf{B}\cdot\text{Cov}(\delta\boldsymbol{\alpha}_{\text{ST}})\cdot\mathbf{B}^T\cdot\mathbf{A}^T + \mathbf{A}\cdot\mathbf{C}\cdot\text{Cov}(\delta\mathbf{f}^b)\cdot\mathbf{C}^T\cdot\mathbf{A}^T \tag{40}$$

where $\mathbf{B} = (\mathbf{C}_f^b)^T(\mathbf{C}_b^s)^T$ and $\mathbf{C}$ transforms accelerometer errors to attitude errors via Eqs. (35)–(36).

This analytical error model enables mission planning by predicting accuracy as a function of latitude, pitch, and sensor specifications, validated by Monte Carlo simulations in Section 5.

5 Simulation Results and Validation

Monte Carlo simulations validate the analytical algorithms and error propagation models developed in the previous sections. This section presents representative results demonstrating positioning accuracy and performance dependencies on key operational parameters. A comprehensive analysis across extended parameter spaces and scenarios will be presented in a forthcoming journal publication.

5.1 Simulation Framework

The Monte Carlo framework ($N_{\mathrm{MC}} = 500$ realizations per scenario) synthesizes sensor measurements incorporating realistic error models and applies the analytical estimation algorithms. Measurements are assumed instantaneous and synchronized, with a static platform (constant position and attitude) during each observation. The simulations consider scenarios where the Sun is within the sun sensor field of view (FOV) and assume clear sky visibility for the star tracker. Sensor error models are assumed to be white Gaussian noise. Error sources include sun sensor angular error ($\sigma_{\mathrm{SS}} = 0.033°$) and star tracker cross-axis and about-axis errors ($\sigma_{\mathrm{ST},xy} = 2$ arcsec, $\sigma_{\mathrm{ST},z} = 10$ arcsec). In addition, AHRS attitude errors ($\sigma_{\mathrm{pitch/roll}} = 0.005°$, $\sigma_{\mathrm{yaw}} = 0.01°$) and deflection of the vertical ($\sigma_{\mathrm{DOV}} = 3$ arcsec, based on EGM2008 model residuals) are added to the nominal attitude when generating the measurements. Scenario consider null latitude ($\phi = 0°$), null vehicle pitch angles and local solar times from morning to afternoon (06:00–12:00) for the sun sensor and from dusk to midnight (08:00–24:00) for the star tracker. Atmospheric refraction corrections employ Bennett's empirical model, and celestial ephemerides are obtained from SPICE JPL DE440 kernels [12]. Performance is characterized by positioning error standard deviation σ_{δ_d} (great-circle distance on WGS84 ellipsoid) and, for star tracker, heading error $\sigma_{\delta\psi}$.

5.2 Sun Sensor Results

Figure 1 presents sun sensor positioning performance for equatorial and mid-latitude observers in level flight. The cumulative error case includes all modeled error sources: sensor measurement uncertainty, stellar aberration, atmospheric refraction, deflection of vertical, and AHRS attitude error.

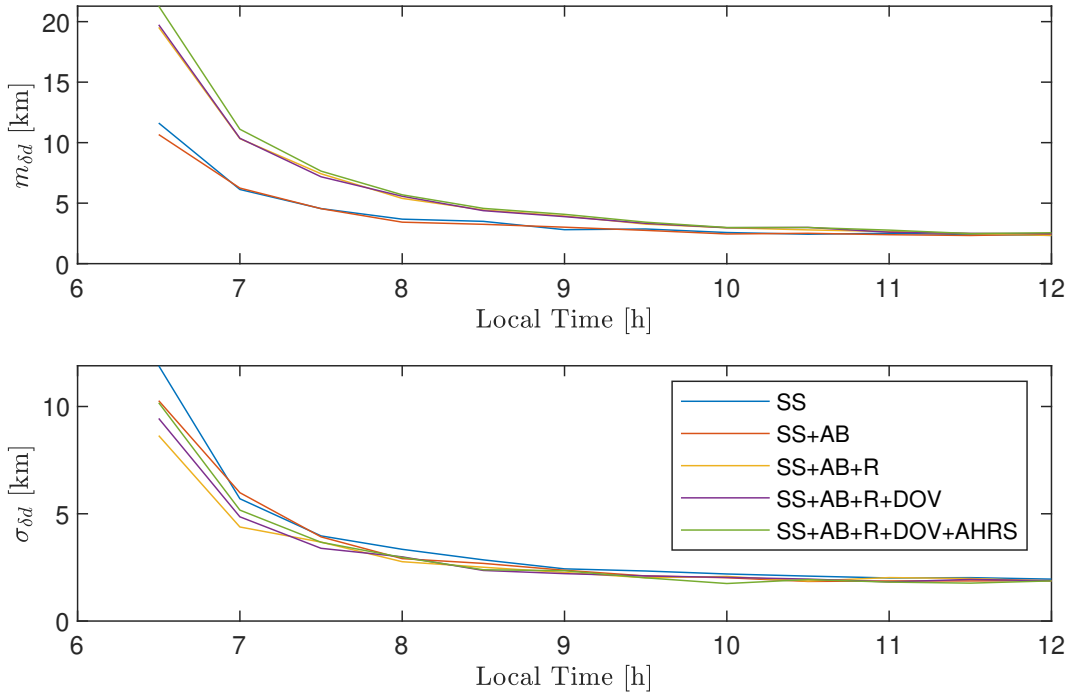

Fig. 1 Sun sensor positioning accuracy versus local solar time for equatorial observer ($\phi = 0°$, $\theta = 0°$). Top: mean error m_{δ_d}. Bottom: standard deviation σ_{δ_d}. Progressive error accumulation shown from sensor-only (blue) to full error budget (green).

Sun sensor positioning achieves standard deviation $\sigma_{\delta_d} \approx 3$–$5$ km during optimal hours (08:00–16:00 local time), dominated by the sensor's 0.033° angular measurement precision. Performance degrades significantly near solar hour angles $H_s = \pm 90°$ (early morning and late afternoon), approaching the singular geometry discussed in Section 3. Atmospheric refraction contributes approximately 2 km to the

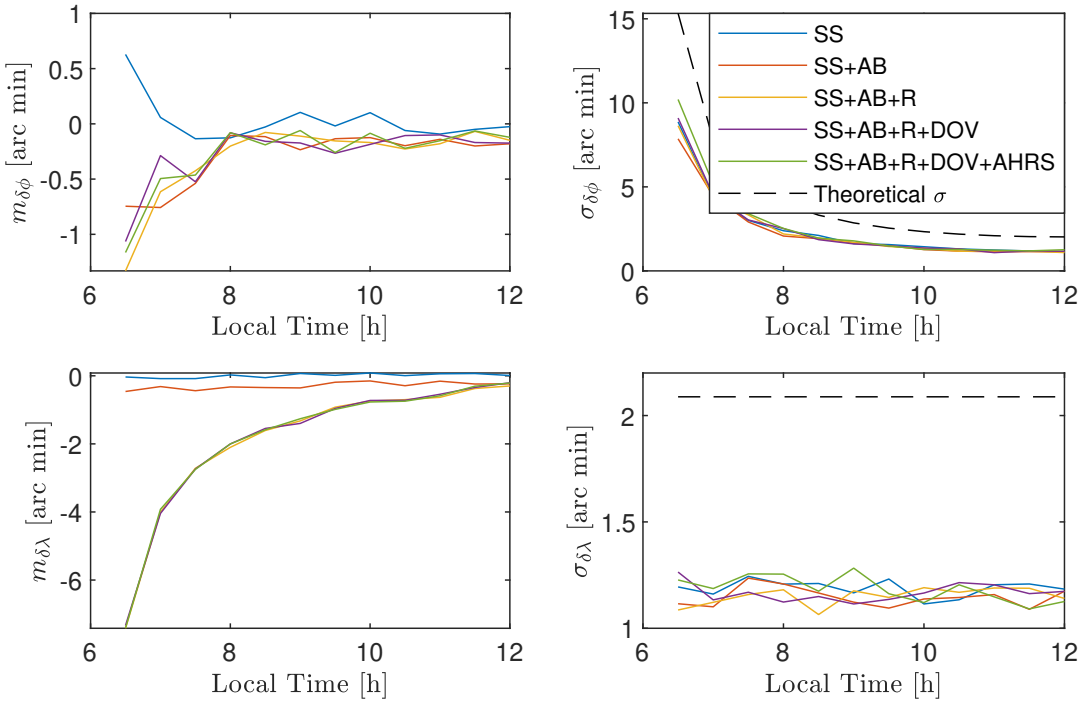

Fig. 2 Sun sensor positioning accuracy, expressed in terms of coordinates error, versus local solar time for equatorial observer ($\phi = 0°, \theta = 0°$). Left: mean error m_{δ_d}. Right: standard deviation σ_{δ_d}. Progressive error accumulation shown from sensor-only (blue) to full error budget (green). Analytical error model shown in dashed line.

error budget, while AHRS attitude uncertainty adds 1–2 km. Deflection of vertical represents a secondary effect at roughly 0.5 km. The hour angle sensitivity represents the primary operational constraint for sun sensor navigation, restricting high-accuracy operation to specific time windows. The analytical error model derived from Jacobian linearization (Eq. (24)) accurately predicts Monte Carlo statistics in non-singular regions, with discrepancies below 15% as evidenced by the theoretical curves presented in Figure 2.

5.3 Star Tracker Results

Figure 3 presents star tracker performance for simultaneous position and heading determination, showing the error decomposition into latitude, longitude, and heading components. Figure 4 presents the positioning error an equatorial observer.

Star tracker navigation demonstrates substantially improved accuracy compared to sun sensors, achieving positioning errors of $\sigma_{\delta_d} \approx$ 340–390 m at equatorial latitudes with sensor error only—an improvement factor of approximately ten. Deflection of vertical correction reduces positioning error by 30–50 m. Unlike sun sensors, star tracker performance exhibits minimal time-of-day variation due to absence of hour angle singularities, enabling continuous operation throughout the day and night. The quaternion-based algorithm provides consistent accuracy across local times, a key advantage for operational flexibility.

The star tracker's most remarkable capability is heading determination, achieving $\sigma_{\delta\psi} \approx 10$ arcsec at the equator (Fig. 3). This precision, driven by the sensor's arcsecond-level angular resolution, enables magnetometer-independent heading reference in magnetically disturbed environments or high-latitude operations where magnetic declination uncertainty is problematic. The analytical error model (Eq. (40)) demonstrates excellent agreement with Monte Carlo statistics across all scenarios, as evidenced by the

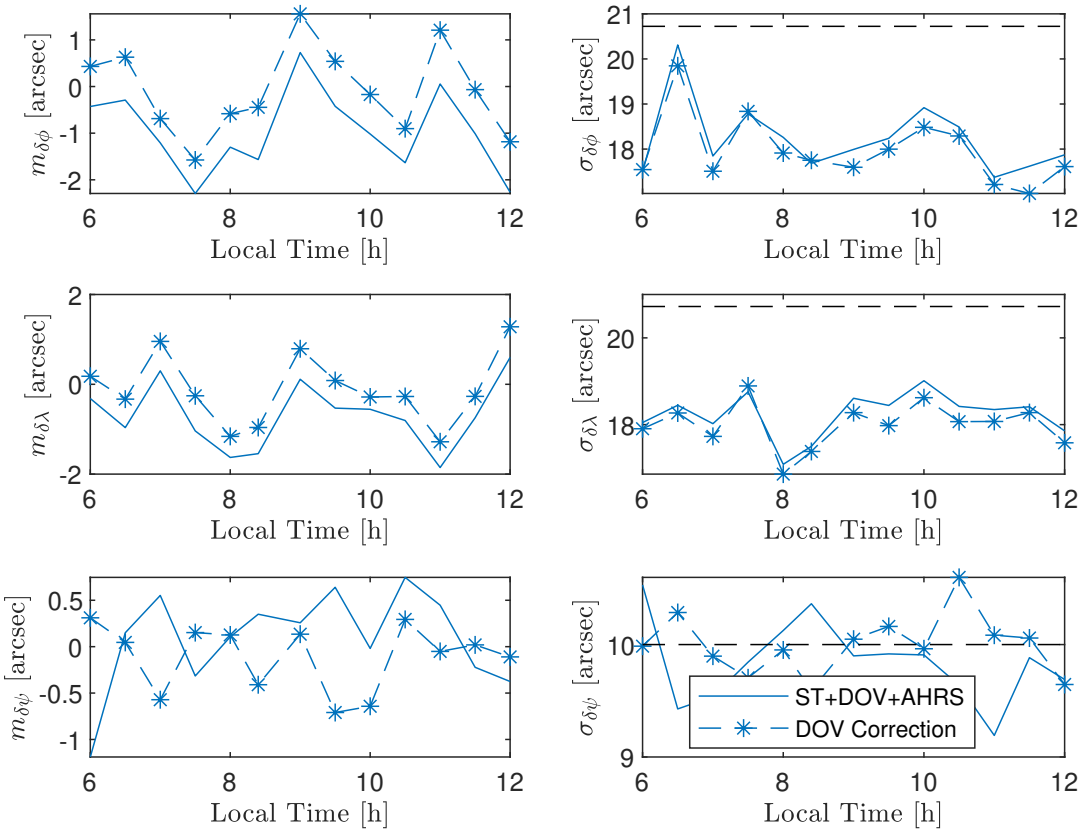

Fig. 3 Star tracker error decomposition for equatorial observer ($\phi = 0°, \theta = 0°$). Rows show latitude error $\delta\phi$, longitude error $\delta\lambda$, and heading error $\delta\psi$. Right column: mean errors. Left column: standard deviations with analytical predictions (dashed curves). Effect of the DOV correction demonstrated.

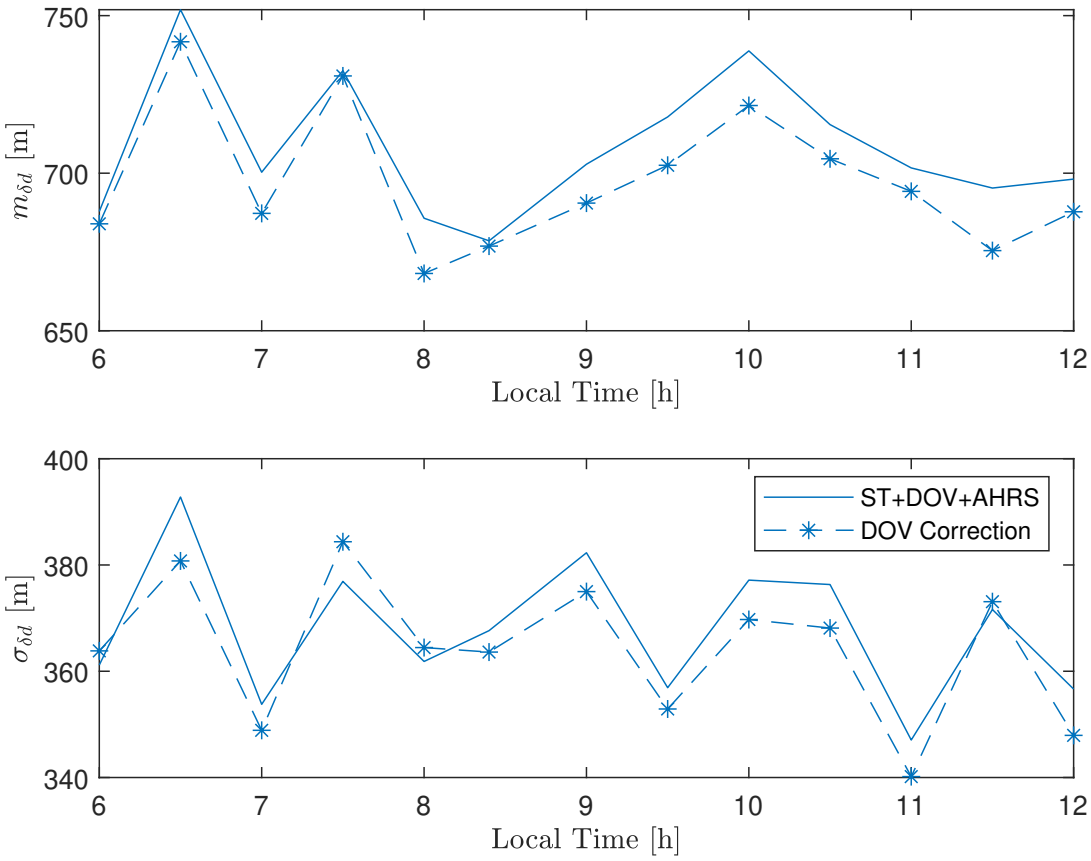

Fig. 4 Star tracker positioning error for equatorial observer ($\phi = 0°, \theta = 0°$). Top: mean errors. Bottom: standard deviation. Effect of the DOV correction demonstrated.

close match between simulation results (solid curves) and theoretical predictions (dashed curves) in the right panels of Figure 4 with maximum discrepancy below 10%.

6 Conclusions

This paper has presented analytical algorithms for GNSS-independent navigation using stellar sensors, providing autonomous position determination through sun sensors and simultaneous position and heading estimation through star trackers. The key contributions include analytical solution procedures enabling real-time implementation, closed-form error propagation models for mission planning, and validation through Monte Carlo simulations incorporating realistic sensor characteristics and geophysical effects.

The sun sensor algorithm achieves positioning accuracies of 3–10 km, limited primarily by the sensor's angular measurement precision and geometric constraints at solar hour angles near ±90°. The approach demonstrates operational feasibility for applications requiring kilometer-level positioning accuracy, particularly during mid-day hours at low to mid latitudes. Error analysis identifies hour angle singularities as the primary operational constraint, with atmospheric refraction and AHRS attitude errors representing secondary contributions to the error budget.

The star tracker algorithm represents the principal contribution of this work, introducing a modified reference frame hierarchy that enables direct extraction of latitude, longitude, and heading through quaternion-based attitude measurements. By incorporating yaw into the Earth-to-navigation transformation, the approach avoids iterative optimization procedures and provides unique analytical solutions through a non-standard 3-2-3 Euler angle sequence. The algorithm achieves sub-kilometer positioning accuracy (100–500 m depending on latitude and pitch) with arcsecond-level heading precision (10–30 arcsec), representing approximately twenty-fold improvement over sun sensor performance. The capability for precise heading determination without magnetic reference is particularly valuable for high-latitude operations or magnetically disturbed environments.

Error propagation analysis via Jacobian linearization accurately predicts Monte Carlo simulation statistics across all tested scenarios, validating the analytical framework for mission planning applications. The analysis quantifies fundamental geometric effects, including the $1/\cos\phi$ latitude amplification factor and hour angle sensitivity, providing design guidelines for operational deployment. Deflection of vertical correction, implemented iteratively using high-resolution geopotential models, improves positioning accuracy by 30–50 meters, with effectiveness increasing at higher latitudes.

Both algorithms exhibit performance degradation at high latitudes due to geodetic coordinate singularities approaching the poles, suggesting alternative parameterizations (e.g., ECEF Cartesian coordinates) for $\phi > 80°$. Vehicle pitch amplifies attitude-dependent errors through trigonometric factors in the transformation chain, motivating selection of tactical-grade or better attitude reference systems for applications requiring high accuracy under dynamic flight conditions.

The analytical approach developed herein provides computational efficiency suitable for real-time embedded implementations while maintaining rigor for error analysis. Future work will address integration with Kalman filtering architectures for optimal fusion with inertial navigation systems, extended validation across broader operational envelopes including near-polar regions and high-dynamic scenarios, and experimental validation through flight testing. The demonstrated capabilities establish stellar navigation as a viable technology for assured PNT in GNSS-denied environments, complementing existing navigation modalities for enhanced resilience in contested operational theaters.

Declaration of Use of Artificial Intelligence

Artificial intelligence was used exclusively to refine the English translation of this article.

References

[1] J.J. Critchley-Marrows and Q. Verspieren, "Ensuring PNT resilience in a time of navigation uncertainty," *Space Policy*, p. 101665, 2024.

[2] C.d.S.M. Aresta, "Resilience of the PNT systems," Ph.D. dissertation, Escola Naval Alfeite, 2017.

[3] T. Rogoway, "SR-71's 'R2-D2' Could Be The Key To Winning Future Fights In GPS Denied Environments," *The War Zone*, Dec. 2017.

[4] D. Cenciotti, "Let's have another look at the B-2's air data ports and astroinertial navigation system," *The Aviationist*, Sep. 2021.

[5] J.-B. Picheloup, "Navigate by the stars—from beneath the waves," *U.S. Naval Institute Proceedings*, vol. 147, no. 10, Oct. 2021.

[6] F. Ting and H. Xiaoming, "Inertial/celestial integrated navigation algorithm for long endurance unmanned aerial vehicle," *Acta Tech. CSAV (Ceskoslov. Akad. Ved.)*, vol. 62, pp. 205–217, 2017.

[7] S. Teague and J. Chahl, "An algorithm for affordable vision-based GNSS-denied strapdown celestial navigation," *Drones*, vol. 8, no. 11, p. 652, 2024.

[8] J. Ali, C. Zhang, and J. Fang, "An algorithm for astro-inertial navigation using CCD star sensors," *Aerospace Science and Technology*, vol. 10, no. 5, pp. 449–454, 2006.

[9] G.G. Bennett, "The calculation of astronomical refraction in marine navigation," *Journal of Navigation*, vol. 35, no. 2, pp. 255–259, 1982.

[10] N.K. Pavlis, S.A. Holmes, S.C. Kenyon, and J.K. Factor, "The development and evaluation of the Earth Gravitational Model 2008 (EGM2008)," *Journal of Geophysical Research: Solid Earth*, vol. 117, no. B4, 2012.

[11] C.H. Acton, "Ancillary data services of NASA's Navigation and Ancillary Information Facility," *Planetary and Space Science*, vol. 44, no. 1, pp. 65–70, 1996.

[12] R.A. Jacobson, "The orbits of the main Saturnian satellites, the Saturnian system gravity field, and the mass of Titan," *Astronomical Journal*, vol. 164, no. 5, p. 199, 2022.